Fusion Engineering and Design 202 (2024) 114409

Contents lists available at ScienceDirect

Fusion Engineering and Design

journal homepage: www.elsevier.com/locate/fusengdes

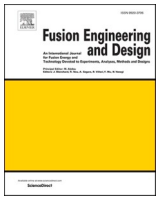

Dispersion interferometry diagnostic at Globus-M2

S.V. Ivanenko [a,*], A.l. Solomakhin [a], P.V. Zubarev [a], A.N. Kvashnin [a], Yu.V. Kovalenko [a], E.A. Puryga [a], V.V. Solokha [a,b], G.S. Kurskiev [b], N.S. Zhiltsov [b], K.D. Shulyatiev [a,b], A.D. Khilchenko [a], V.B. Minaev [a,b], P.A. Bagryansky [a]

[a] Institute of Nuclear Physics G.I. Budker SB RAS, Novosibirsk, Russia
[b] Ioffe Physical-Technical Institute RAS, St. Petersburg, Russia

ARTICLE INFO

Keywords:
Plasma diagnostic
Dispersion interferometer
Thomson scattering
Data acquisition systems
Globus-M2 tokamak
Plasma density control

ABSTRACT

The dispersion interferometry diagnostic (DI) based on the CO_2-laser was commissioned at the Globus-M2 tokamak for absolute measurements of the line-integrated electron density (IED) along the chord in the equatorial plane. IED measurement error corresponding to the intrinsic noise of the acquisition device was below 10^{17} m^{-2} with time and spatial resolution 20μs and 2 cm, respectively. Inference of the IED using the second harmonic interference was done by means of spectral algorithm. Execution of the algorithm is performed at the FPGA in real-time mode. During the year long operation, DI was proven to be reliable and robust IED diagnostic at Globus-M2.

1. Introduction

The interferometry diagnostic is widely used in plasma physics experiments as a robust instrument for line-integrated electron density (IED) measurements. Interferometry is using superimposed waves to infer the optical path difference for two optical channels. Traditionally used Michelson and Mach-Zehnder interferometers rely on the spatial separation of the reference and sample channels. Dispersion interferometer (DI) separates reference and sample channels in frequency which allows for measurements in mediums with chromatic dispersion, plasma in particular. Reference and sample beams are travelling along the same optical path, as the sample beam is produced by the nonlinear frequency doubling optical component. As the result, DI is weakly sensitive to the vibrations of the optical components which frequently accompany present-day fusion plasma experiment devices with relatively large dimensions and magnetic field magnitudes. The fundamental harmonic beam (reference beam) after passing the plasma is upconverted to the second harmonic right before the detection. The detection of the superimposed second harmonic waves of reference and sample beams is a principal difference between DI and two-color interferometers using two separate lasers. The intensity of the detected superimposed wave is described by the Eq. (1).

$$I = I_1 + I_2 + 2\sqrt{I_1 I_2} sin(\Delta\varphi), \tag{1}$$

where I_1, I_2 – intensity of the superimposed second harmonic wave, $\Delta\varphi$ – phase difference proportional to the IED (Eq. (2)).

$$\Delta\varphi = \frac{1}{4\pi\varepsilon_0}\frac{3}{2}\frac{e^2}{mc^2}\lambda\int_0^L n_e dl, \tag{2}$$

where e – elementary charge, m — electron mass, c — speed of light, λ – wavelength of the fundamental harmonic. The wavelength of the CO_2-laser (λ ≈ 10 μm) is low enough to assume refraction influence on the measurements negligible.

DI diagnostics based on the CO_2-laser currently operating at the GDT (Novosibirsk, Russian Federation) [1], Wendelstein 7-X (Greifswald, Germany) [2,3], LHD (Toki, Japan) [4] devices, and was previously used at TEXTOR (Jülich, Germany) [5].

Spherical tokamak Globus-M2 (Saint-Petersburg, Russian Federation) is the unique scientific device for high-temperature plasma confinement and heating research in low-aspect ratio tokamaks. The prominent spherical tokamak application is the construction of the compact fusion neutron source (CFNS) [6–10]. One of the key requirements for the CFNS is the real-time plasma density control in discharges longer than 0.5 s. The plasma density control is needed to mitigate Alfven modes; to reduce the heat load at the plasma facing components, such as divertor plates; to sustain the high fast particle

* Corresponding author.
E-mail address: S.V.Ivanenko@inp.nsk.su (S.V. Ivanenko).

https://doi.org/10.1016/j.fusengdes.2024.114409
Received 6 October 2023; Received in revised form 15 March 2024; Accepted 1 April 2024
Available online 9 April 2024

density.

The Globus-M2 electromagnetic system is capable of plasma discharges with duration up to 0.7 s [6]. The plasma density control is the necessary prerequisite for sustenance of high duration discharge, which is not possible to achieve without addressing three key points. Firstly, Globus-M2 high-density discharges exhibit the line-average density around $10^{20}m^{-3}$ at submaximal values of plasma current. At such high electron densities, the microwave interferometry diagnostic accuracy is at the unsatisfactory levels due to the refraction. Secondly, the total gas input is governed by the recycling and due to the low pumping capabilities in the open divertor configuration, the density is hard to control. The control can be regained for a limited amount of discharges by wall conditioning using baking and boronization. Thirdly, the plasma density heavily affects the heating and non-inductive current generation efficiencies [11–13].

For real time IED measurements during the plasma discharge at Globus-M2 the CO_2-laser based DI diagnostic with external phase modulation was chosen. The Globus-M2 DI development was conducted using authors' experience in the DI development at GDT [1] and TEXTOR [5]. The DI signal detection and real-time IED estimation were provided by newly developed phasemeter based on a fast ADC module developed in Budker Institute of Nuclear Physics [14]. The temporal and spatial resolution of the DI at Globus-M2 is 20 μs and 2 cm, respectively. The measurement error is below $10^{17}\ m^{-2}$. During the year long operation DI was proven to be reliable and robust IED diagnostic at Globus-M2. The ongoing task is to add DI to the real-time feedback loop for plasma density control.

The paper is sectioned as follows. The Section 1 describes the optical scheme of the DI diagnostic. Section 2 details algorithm of the IED reconstruction based on the spectral decomposition of the superimposed wave power. Section 3 and 4 presents a measurement module of the DI and its calibration procedure. Section 5 shows experimental IED measurements during the Globus-M2 campaign and compares the DI results with Thomson scattering and microwave interferometry diagnostics.

2. DI at globus-m2

The optical scheme of the dispersion interferometer at Globus-M2 tokamak is shown in Fig. 1. The majority of optical components is positioned on the optical table (1 in Fig. 1) in 2 m distance from the tokamak (2 in Fig. 1). The vacuum vessel is equipped with the optical windows made of ZnSe (3 in Fig. 1). The corner reflector and supporting stand are marked as 4 in Fig. 1. The light source is adjustable CO_2-laser Access Laser AL50SG (5 in Fig. 1) set up to radiate at wavelength of $\lambda CO_2 = 9.6$ μm. The laser beam travels through aperture (6 in Fig. 1) reducing the back reflections intensity, and through the germanium wedge at Brewster angle (7 in Fig. 1). Part of the laser beam is split into the DEXTER ST150 detector for laser output power control. The emission which directed into the laser from the optical scheme is reflected from other side of the wedge and measured by the other DEXTER ST150 detector (9 in Fig. 1). Multiple times reflected beams are being dissipated by the conical apertures (10 in Fig. 1). The majority of the laser emission passes the mechanical shutter (11 in Fig. 1). Out of consideration for stability the laser operates in continuous mode and due to safety reasons the mechanical shutter opens only during the IED measurements, in stand by conditions shutter reflects beam into water cooler absorber. The spherical mirror (12 in Fig. 1) focuses ≈20 W beam in nonlinear frequency doubler $ZnGeP_2$ (13 in Fig. 1). This crystal $4 \times 5 \times 5$ mm^3 (HxWxL), θ_{cut}=30° made according to our drawing by the "Otical Crystal Laboratory" Tomsk, Russia (loc-ltd.com). Beam reflected by doubler surfaces is absorbed by the optical trap (14 in Fig. 1). After the frequency doubler the fundamental ≈9 W and second ≈8 mW (theoretical value) harmonic emission travels along the same path to the spherical mirror (15 in Fig. 1) and through the elasto-optic modulator Hinds Instruments PEM-200 II/ZS50 (16 in Fig. 1). The elasto-optic modulator is made of a plane-parallel ZnSe plate which is being compressed/decompressed from two sides by piezoelectric elements. During the deformation procedure the ZnSe losses its isotropy and becomes anisotropic and exhibit dispersion for fundamental and second harmonics resulting in phase shift between superimposed second harmonic beam at the detector. The 50 kHz sine voltage is applied to piezoelectric elements which allows for robust phase shift reconstruction. After the modulation beams enters the plasma through the vacuum windows (3 in Fig. 1) twice due to the corner reflector (4 in Fig. 1). Vacuum windows are made of the anti-reflective coated ZnSe glass. Vacuum windows are protected during the wall-conditioning low-temperature plasma discharge by vacuum shutters. Corner reflector is shifted to 2 cm for provide vertical position difference between the incident and reflected beams. This allows these beams to be separated using a special low height mirror (18 in Fig. 1). The reflected beam reaches optical table and travels to the second frequency doubler (20 in Fig. 1) via several mirrors. This crystal $4 \times 6 \times 5$ mm^3 also manufactured by the "Otical Crystal Laboratory". The nonlinear frequency doubler partially transforms fundamental harmonic ≈8 W to the second harmonic, while the second harmonic from the first doubler remains the same due to the low power as it 10^{-3} times lower than fundamental harmonic power. Further three beams follow the same path. The emission reflected from the one of the surfaces of the frequency doubler is absorbed by optical trap (21 in Fig. 1). The emission from the other side of the doubler reaches the five beam position detectors DEXTER ST150 aligned perpendicular to the

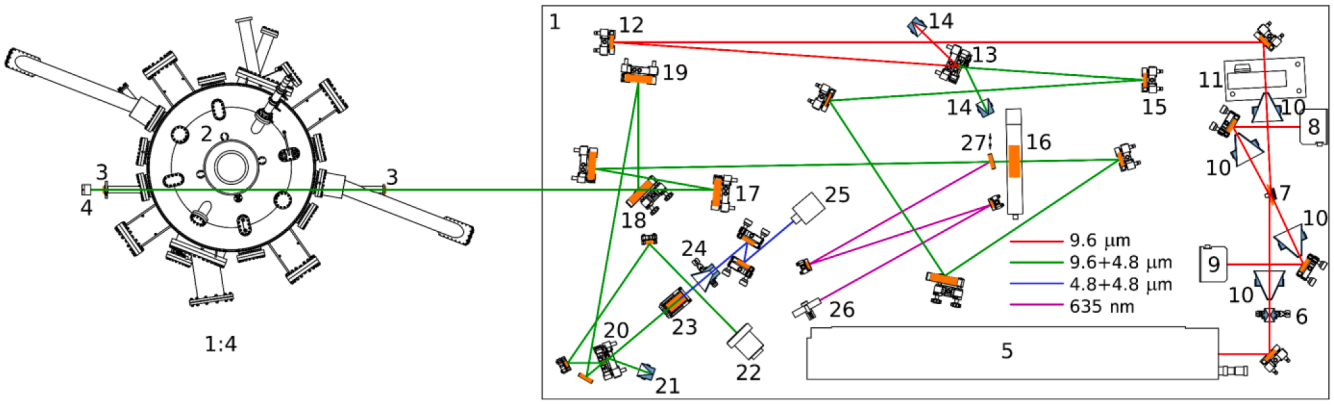

Fig. 1. The optical scheme of the dispersion interferometry diagnostic (The Globus-M2 vacuum vessel is downscaled fourfold). 1 — optical table, 2 — Globus-M2 vacuum vessel, 3 — window, 4 — corner reflector, 5 — laser, 6 —aperture, 7 — Brewster wedge, 8 and 9 — λ=9.6 μm detectors, 10 — cone aperture, 11 — shutter, 12 — spherical mirror, 13 — frequency doubler, 14 — optical trap, 15 — spherical mirror, 16 — elasto-optic modulator, 17 — spherical mirror, 18 — low height mirror, 19 — spherical mirror, 20 — frequency doubler, 21 — optical trap, 22 — beam positioning detector, 23 — optical filter, 24 — cone aperture, 25 — λ=4.8 μm detector, 26 — visible laser; 27 - flat mirror which combines the visible and CO2-laser beams.

beam in cross-like shape. The position detector usage is restricted by alignment monitoring during the operation. The three beams lands on the wavelength filter made of LiF wedge (23 in Fig. 1) at Brewster angle which absorb the fundamental harmonic emission while being fully transparent for the second harmonic. Emission which is reflected from the filters surfaces is absorbed cone aperture (24 in Fig. 1). The filtered beams power of several mW (theoretical value) is focused on the VIGO System PVI-4TE detector by means of two spherical mirrors. The detected signal is processed by the measurement module which reconstructs the IED. Total beam path length from laser to detector ≈15 m. The part of this path that is sensitive to dispersion and potentially vibration is located between the frequency doublers and is ≈12 m. Changed in atmospheric characteristics (path ≈7 m) such as temperature, pressure and humidity affect its dispersion [15] and can give a false signal. However, during the plasma discharge at Globus-M2 ~1 s these changes are not significant.

The initial alignment of the DI beam path requires the visible laser usage (26 in Fig. 1). By means of two spherical mirrors the beam is directed at the flat mirror (27 in Fig. 1) which combines the visible and CO_2-laser beams. The final alignment is done with CO_2-laser beam.

3. IED reconstruction algorithm

The classical DI scheme imply that detector signal from the superimposed second harmonic waves is described by the Eqs. (1) and 2 [1]. To achieve the robust phase shift Δφ calculation with non-monotonic signal dependency on the Δφ (Eq. (1)) the elasto-optic modulator (EOM) was used (Fig. 1). EOM changes phase of the passing radiation according to the applied sine wave voltage. As the result, the equation describing power of the signal at the detector exhibit the oscillating term:

$$I = I_1 + I_2 + 2\sqrt{I_1 I_2}\sin(M sin(\Omega t) + \Delta\varphi), \tag{3}$$

where M — modulation index, Ω — modulation frequency. At M values higher than π the detector signal span the whole dynamic range independently of phase shift value.

There are several hardware implementation methods of phase shift reconstruction algorithm from the detector and modulator signals. In particular, paper [16] presents FPGA implementation utilizing the amplitude-time signals. In assumption, that I_1 and I_2 intensities are constant during the modulation period the time-independent component of signal can be neglected, thus time-dependent component amplitude is scaled by min-max normalization. In this case, phase shift at zero sine values, corresponding to the maximal sensitivity of the DI is proportional to the magnitude of the modulation signal:

$$\Delta\varphi = |M sin(\Omega t)|. \tag{4}$$

Despite the easy implementation this amplitude-time signal analysis method has several drawbacks. First of all, the IED reconstruction accuracy strongly depends on the noise amplitude. Noise sources corrupting the detector signal as follows:

- Laser output power fluctuations;
- Temperature fluctuations and errors in nonlinear doubler positioning;
- Changes in total transmission of the optical path;
- Large-scale beam misalignment comparable with detector aperture.

These events might take place due to the refraction at high density gradients or during high dynamic loads, for instance during the disruption.

Events presented below also corrupt time-amplitude signal and lead to additional errors in DI estimation:

- Excessive or insufficient modulation depth of the probing beam phase;
- Additional phase shift in elasto-optic modulator due to the temperature fluctuations and acoustic resonances;
- The back reflected stray light interference with main light inside laser;
- Rapid phase change when laser generation transitions to an adjacent line .

These events are leading to additional errors in phase shift estimations, and thus, the IED. Therefore, during the development of the DI diagnostic the decision was made to substitute the time-amplitude analysis algorithm for spectral analysis algorithm. The phase shift reconstruction algorithm described in [17] was taken as a basis.

In Fourier space the intensity of superimposed signal is represented by Eq. (5):

$$V(t) = V_{DC} + V_{AC}\cos[M\sin(\Omega t) + \Delta\varphi)]. \tag{5}$$

The cosine decomposition leads to Eq. (6):

$$V(t) = V_{DC} + V_{AC}\cdot\{\cos(\Delta\varphi)\cdot\cos[M\sin(\Omega t)] - sin(\Delta\varphi)\cdot\sin[M\sin(\Omega t)]\}. \tag{6}$$

Let's use the expressions:

$$\cos[M\sin(\Omega t)] = J_0(M) + 2\sum_{n=1}^{\infty} J_{2n}(M)\cos[(2n)\cdot\Omega t], \tag{7}$$

$$\sin[M\sin(\Omega t)] = 2\sum_{m=1}^{\infty} J_{2m-1}(M)\sin[(2m-1)\cdot\Omega t], \tag{8}$$

where $J_n(x)$ is the Bessel function of the first kind of order n

Substitution of Eq. (7) and 8 in Eq. (6) leads to signal decomposition shown in Eq. (9):

$$\begin{aligned} V(t) = {} & [V_{DC} + V_{AC}\cdot\cos(\Delta\varphi)\cdot J_0(M)] - \\ & - 2\,V_{AC}\sin(\Delta\varphi)\cdot J_1(M)\sin(\Omega t) + \\ & + 2\,V_{AC}\cos(\Delta\varphi)\cdot J_2(M)\cos(2\Omega t) - \\ & - 2V_{AC}\sin(\Delta\varphi)\cdot\sum_{m=2}^{\infty} J_{2m-1}(M)\sin[(2m-1)\cdot\Omega t] + \\ & - 2V_{AC}\cos(\Delta\varphi)\cdot\sum_{n=2}^{\infty} J_{2n}(M)\cos[(2n)\cdot\Omega t]. \end{aligned} \tag{9}$$

The amplitude of first and second harmonic of V(t) is expressed as below $V(t)$:

$$V_{\Omega}(\mathrm{t}) = -2V_{AC}\sin(\Delta\varphi)\cdot J_1(M)\sin(\Omega t)\ ,$$

$$V_{2\Omega}(\mathrm{t}) = 2V_{AC}\cos(\Delta\varphi)\cdot J_2(M)\cos(2\Omega t)\ .$$

First and second harmonic contains enough information to calculate phase shift, the influence of V_{AC} is reduced by using the harmonic amplitude ratio:

$$\frac{J_2(M)}{J_1(M)}\frac{V_{\Omega}(\mathrm{t})}{V_{2\Omega}(\mathrm{t})} = \frac{|\sin(\Delta\varphi)|}{|\cos(\Delta\varphi)|} = |\mathrm{tg}(\Delta\varphi)| \tag{10}$$

The Eq. (10) states that phase shift $\Delta\varphi$ depends on the first and second harmonic amplitude ratio and modulation depth M only. The amplitude ratio is calculated using the discrete Fourier transform at each modulation period. With assumption of constant modulation depth during the modulation period, the phase shift $\Delta\varphi$ is calculated by inverse tangent function in the range $[0,\pi/2]$.

3.1. The modulation depth calculation

The Eq. (10) contains the term $|\frac{J_2(M)}{J_1(M)}|$, which depends on the modulation depth M. The necessity of the modulation depth calculation is

driven by its inconsistency during the experiment. The phase shift reconstruction algorithm described in [17] does not take into account changes in modulation depth. Therefore the algorithm required modification. At Globus-M2 DI average modulation depth is a function of voltage magnitude applied to the modulator. Its value is in range fromπ /2 to π . The real-time estimation of the Bessel functions ratio is done by calculating intensities of the first and third harmonic amplitude ratio. According to (9), they are related to the modulation depth and phase shift as:

$$V_{\Omega}(\mathrm{t}) = -2V_{AC}\sin(\Delta\varphi)\cdot J_1(M)\sin(\Omega t)\ ,$$

$$V_{3\Omega}(\mathrm{t}) = -2V_{AC}sin(\Delta\varphi)\cdot J_3(M)\sin(3\Omega t)\ .$$

The real-time estimation of M through the Bessel functions ratio is done by calculating intensities of the first and third modulation harmonic amplitude ratio:

$$\left|\frac{V_{\Omega}(t)}{V_{3\Omega}(t)}\right| = \left|\frac{J_1(M)}{J_3(M)}\right| \tag{11}$$

The value of the term $|\frac{J_2(M)}{J_1(M)}|$ required for (10) can be determined using value of the modulation depth M .

3.2. The phase shift extension algorithm

The Eq. (10) allows us to calculate phase only in range from 0 to π /2 To extend the range algorithm uses additional information about the first and second harmonic signs:

$$V_{\Omega}(\mathrm{t}) = -2V_{AC}\sin(\Delta\varphi)\cdot J_1(M)\sin(\Omega t)\ ,$$

$$V_{2\Omega}(\mathrm{t}) = 2V_{AC}\cos(\Delta\varphi)\cdot J_2(M)\cos(2\Omega t)\ .$$

Due to positive values of Bessel functions in range $\pi \pm \pi$ /6, the sign is governed by sine and cosine of phase shift only. The phase sign and quarter period indices as shown in Table 1.

At high plasma densities, the phase shift can exceed 2π. Due to the periodicity of the cosine (expression (6)), a phase jump occurs at this point, which leads to the loss of information about the total phase shift. This feature imposes a limitation on the rate of phase change: for one modulation period (20 μs) no more than π/2. This corresponds to a change in the average linear density of $\approx 4 \times 10^{19}\ m^{-2}$, which in turn corresponds to a change in plasma density of $4 \times 10^{17}\ m^{-3}$ in 20 μs over a characteristic length of 1 m. This is several times greater than those changes in density, which are observed in modern plasma installations under normal conditions [18]. In principle, this limitation can be overcome by using a shorter wavelength laser or a higher modulation frequency.

4. Data acquisition and processing system

Described in the previous section phase shift reconstruction algorithm is implemented in double-channel universal digital measurement module. The module scheme is shown in Fig. 2. It has two input ports: measurement input and synchronization input, which are connected with output port of VIGO System PVI-4TE detector and base synchronization signal of the elasto-optic modulator. The measurement input signal is digitized with 14-bit ADC (AD9255) with sample frequency 12.8 MSamples/s synchronized with signal of the elasto-optic modulator. The series of the ADC output samples (256 samples per modulation period) is transferred to the data processing node based on the Intel FPGA Cyclone V. The FPGA contains ARM9 processor core, random-access memory controller 1GB DDR3 and network controller Ethernet-1000. The data processing node execute phase shift reconstruction algorithm, writes measurement results in the memory (every 20 μs) and transfers this data to the master server by Ethernet protocol. This node listens the master server port and process the control packets which setting operation mode and miscellaneous settings (transmission coefficient, preamplifier bandwidth, input signal base level, registration time window and others).

The measurement module saves the phase shift data and raw ADC samples in time window up to 0.8 s.

Table 1
Definition of phase shift quarter.

	$V\Omega+$	$V\Omega-$
$V\Omega+$	I	II
$V\Omega-$	IV	III

5. Validation of DI operation and measurement accuracy assessment

Before the Globus-M2 experimental campaign the operation of DI was validated using the oscillating wedge in the optical path before the first vacuum window. The wedge is connected to the crank mechanism, which reciprocate it with 0.4 second period and 7.2 ± 0.2 mm magnitude. The 1° wedge was made of BaF_2. The refractive index of BaF_2 at $\lambda =$ 9.6 μm is $n = 1.45$ and at $\lambda = 4.8$ μm is $n = 1.40$, therefore the expected phase shift during the full period is expected to be equal to 8.1 ± 0.2 rad. The value measured by DI matches the expected value. Fig. 3 presents the time dependency of the phase shift during the reciprocating wedge movement.

It was decided to evaluate the DI noise directly during the operation of the tokamak. We consider this approach to be the most correct, since during the operation of all tokamak systems, displacements of the interferometer probing beams relative to optical elements with dispersion are possible. Fig. 4 shows typical IED time series during discharge by DI (black line). We calculated the root mean square noise until the plasma appeared in the period 0.1–0.17 s. It was estimated at $\sim 10^{17}\ m^{-2}$.

6. Results of DI operation in Globus-M2 experiments

DI diagnostic has been operating at Globus-M2 tokamak since September 22, 2022. By April 11, 2023, the dispersion interferometer had attempted line integrated electron density (IED) measurements in 451 discharges. In 424 (94.1%) of discharges, measurements were successful; in 26 (5.4%) discharges, measurements were failed due to the operator's mistake and synchronization failure; and in 1 (0.2%) pulse, the measurements were faulty due to the laser power drop.

The comparison of the dispersion interferometer measurements with other diagnostics requires the calculation of the effective chord length inside the last closed flux surface (LCFS) of the plasma. The LCFS in Globus-M2 is calculated by means of the current filament method [19], which allows quick estimation of the LCFS. The measurements take place in the equatorial plane of the Globus-M2 tokamak with a distance from the center of the tokamak of $l = 0.17$ m; thus, the calculation of the chord length is:

$$L = \sqrt{\left(R_{in}^2 - l^2\right)} - \sqrt{\left(R_{out}^2 - l^2\right)}, \tag{12}$$

where R_{in} and R_{out} are the inner and outer radii of the torus, respectively.

The full range of measured chord lengths (2.17 m at the 10% percentile, 2.31 m at the 90% percentile) and line-integrated electron densities ($1.8{\cdot}10^{19}\ m^{-2}$ at 10% percentile, $1.1{\cdot}10^{20}\ m^{-2}$ at 90% percentile) are shown in Fig.5a and Fig. 5b. The measured IEDs are confidently inside the technical limits ($5{\cdot}10^{17}$ - $3{\cdot}10^{20}\ m^{-2}$). The lower limit is practically unreachable in Globus-M2 tokamak plasma during baseline operation. The upper limit is reachable even before the Greenwald density [20] ($n_e^{GD} \sim 3{\cdot}10^{20}\ m^{-3}$) due to the long

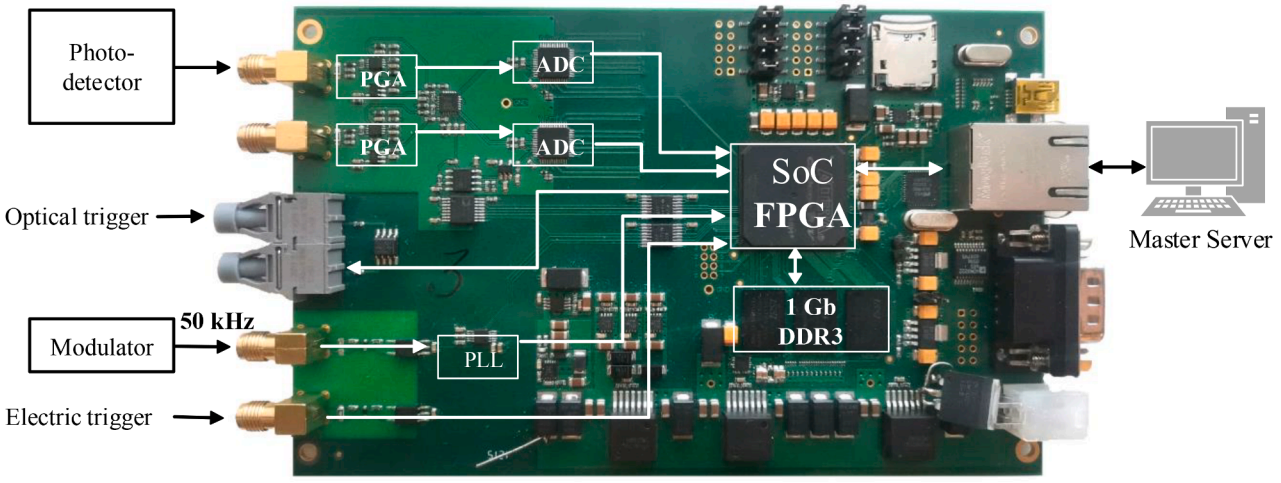

Fig. 2. Universal digital measurement module (phase meter).

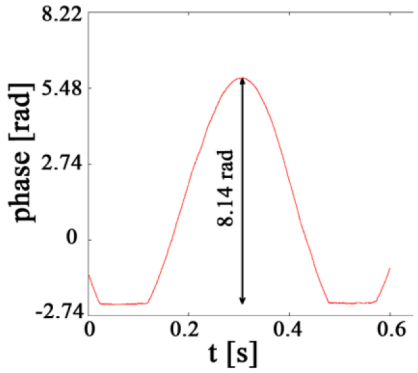

Fig. 3. Validation of DI operation by means of optical wedge.

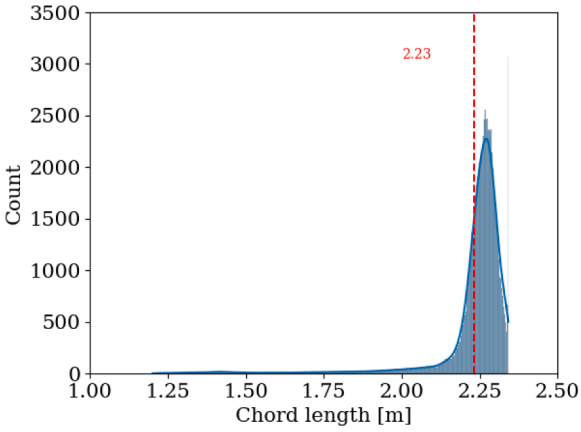

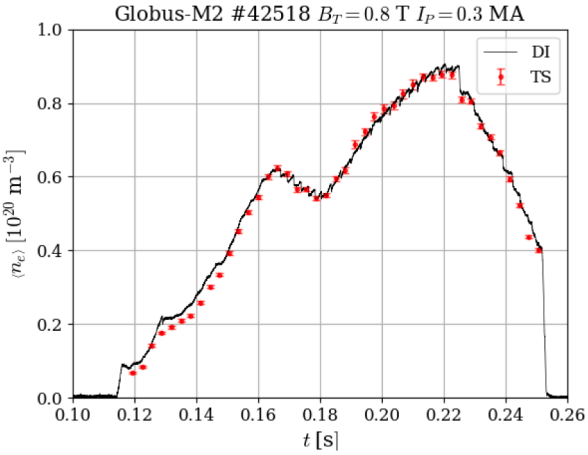

Fig. 4. IED time series during discharge #42,518 by DI (black line) and Thomson scattering (red markers).

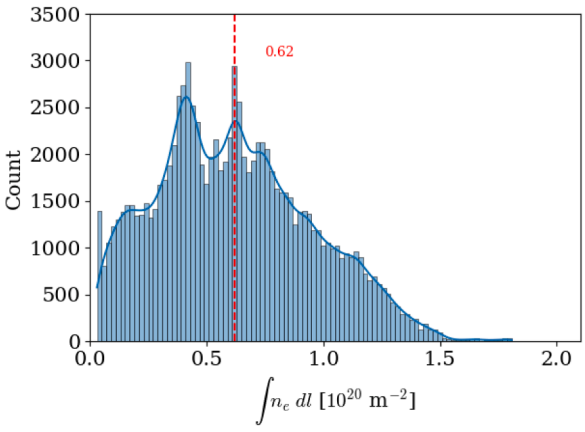

Fig. 5. a Distribution of the DI chord lengths (blue histogram); the mean value position is marked by a red dashed line. b. Distribution of the DI IEDs (blue histogram); the mean value position is marked by a red dashed line.

measurement chord. Although, the highest IED achieved during the DI operation was approximately $1.8{\cdot}10^{20}\ m^{-2}$ (Fig. 5).

The electron density at Globus-M2 is being measured by three diagnostic systems: the DI, the microwave interferometry [21], and the Thomson scattering (TS) diagnostic. The microwave interferometry utilizes the vertical measurement chord, so the direct comparison is largely complicated. Also, the microwave beam experiences refraction and phase jumps at high densities and therefore has the tendency to underestimate the electron density. The TS measures the electron density profile in the equatorial midplane while being absolutely calibrated by the Raman scattering method. As a result, it provides the most robust reference for IED comparison. The IED for TS diagnostics is calculated using the magnetic flux surface reconstruction and numerical integration over the flux surfaces. The magnetic flux surfaces are approximated by equations [22]:

$$R(a) = R_g + \Delta(a) + a\big(cos(\theta) - -\delta(a)\cdot sin^2(\theta)\big)$$

$$Z(a) = \Delta Z + a\cdot k\cdot sin(\theta)$$

where R_g is the radius of the geometric center of the plasma pinch, Δ is the Shafranov shift of the magnetic surface, a is the minor radius of corresponding magnetic surface, θ is the poloidal angle, δ is the plasma triangularity, ΔZ is the plasma pinch shift along the vertical axis Z, and k is the elongation.

TS IED and DI IED are in good agreement as the deviation is lower than 10%. The comparison of IEDs in pulse #42,518 is shown in Fig. 4. The ratio of the TS and DI chord averaged electron densities over more than 30 pulses of the 2022–2023 experimental campaign is shown in Figs. 6 and 7.

The average IEDs ratio is 0.95, which is lower than unity due to the initial phase of discharges; the standard deviation is around 0.08. The deviation consists of two terms: the systematic deviation during the startup phase at low densities and the random deviation. Fig. 7 shows the dependence of ratios on the averaged electron density. The electron density inferred with the Thomson scattering diagnostic shows approximately 5% random deviation and around 10% systematic deviation at the electron densities below $n_e = 3{\cdot}10^{19}\, m^{-3}$. Therefore, we can conclude that DI IED measurements are robust and consistent with TS measurements, as the DI to TS IEDs ratio has a homoscedastic distribution.

7. Conclusion

The result of Budker Institute of Nuclear Physics and Ioffe Physico-Technical Institute collaboration was the development of the dispersion interferometer based on a CO_2 laser for measuring the absolute values of the plasma electron density in the Globus-M2 tokamak. The time resolution of the DI is 20 μs, the spatial resolution is 0.02 m, and the measurement accuracy, determined by the noise component amplitude of the recorded signal, is no worse than $10^{17}\, m^{-2}$.

During the year long operation, DI has proven to be reliable and robust IED diagnostic at Globus-M2 tokamak. It is planned to use this device as a detector for building a system for plasma density stabilizing in Globus-M2 in future.

Funding

This work was supported by the grant of the Russian Science Foundation No. 21–79–20201.

CRediT authorship contribution statement

S.V. Ivanenko: Writing – review & editing, Writing – original draft, Visualization, Software, Project administration, Methodology. **A.l. Solomakhin:** Formal analysis, Investigation, Methodology, Visualization, Writing – original draft, Writing – review & editing. **P.V. Zubarev:** Software. **A.N. Kvashnin:** Methodology. **Yu.V. Kovalenko:** Software. **E.A. Puryga:** Validation. **V.V. Solokha:** Investigation, Formal analysis. **G.S. Kurskiev:** Investigation. **N.S. Zhiltsov:** Investigation. **K.D. Shulyatiev:** Investigation. **A.D. Khilchenko:** Formal analysis, Conceptualization. **V.B. Minaev:** Supervision, Project administration, Conceptualization. **P.A. Bagryansky:** Writing – review & editing, Writing – original draft, Supervision, Project administration, Conceptualization.

Declaration of competing interest

The authors declare that they have no known competing financial interests or personal relationships that could have appeared to influence the work reported in this paper.

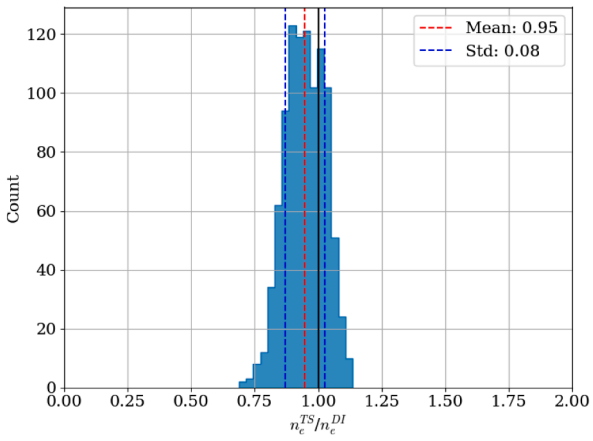

Fig. 6. The distribution of the average electron density ratio by DI and TS (blue histogram): a black solid line marks unity, a red dashed line marks the mean value position, and blue lines mark the standard deviation positions.

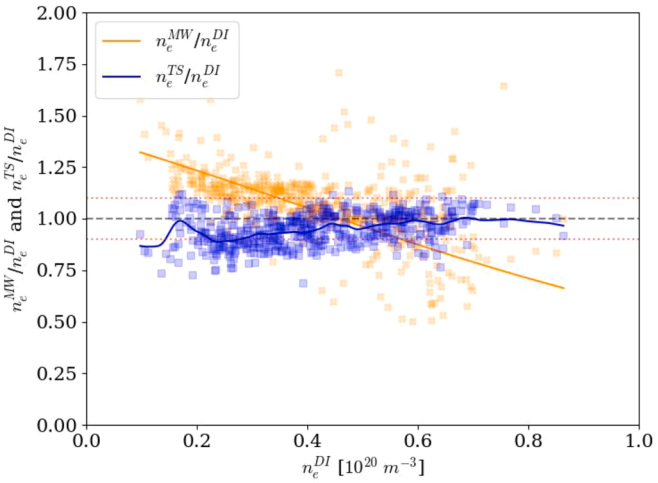

Fig. 7. The dependency of average electron density ratios by DI and TS (blue) and by DI and MW (orange) Solid lines are provided by Gaussian process regression. The black dashed line marks unity, and the red dotted lines mark 10% deviation positions.

Data availability

Data will be made available on request.

References

[1] A.L. Solomakhin, P.A. Bagryanskii, R.V. Voskoboinikov, P.V. Zubarev, A. N. Kvashnin, A.A. Lizunov, V.V. Maksimov, A.D Khil'chenko, A dispersion interferometer based on a co2 laser, – Instrum. Experim. Techn. 48 (5) (2005) 649–658. N°.

[2] J. Knauer, et al., Power balance analysis of wendelstein. — In: 7-X Plasmas Using Profile Diagnostics 43rd EPS Conference on Plasma Physics, 2016, p. 4.017.

[3] K.J. Brunner, T. Akiyama, M. Hirsch, J. Knauer, P. Kornejew, B. Kursinski, H. Laqua, J. Meineke, H. Trimiño Mora, R.C. Wolfa, the W7-X team, Real-time dispersion interferometry for density feedback in fusion devices, J. Instrum. 13 (09) (2018) P09002.

[4] T. Akiyama, R. Yasuhara, K. Kawahata, K. Nakayama, S. Okajima, K. Urabe, K. Terashima, N. Shirai, Development of dispersion interferometer for magnetic confinement plasmas and high-pressure plasmas, J. Instrumen 10 (2015) P09022.

[5] H. Dreier, P. Bagryansky, N. Baumgarten, W. Biel, H.T. Lambertz, M. Lehnen, A. Lizunov, A. Solomakhin, First results from the modular multi-channel dispersion interferometer at the TEXTOR tokamak, Rev. Scient. Instrum 82 (2011) 063509. p.

[6] V.B. Minaev, et al., Spherical tokamak Globus-M2: design, integration, construction, Nucl. Fusion 56 (6) (2017) 066047. N°6 ArtNo: N°.

[7] G.S. Kurskiev, et al., The first observation of the hot ion mode at the Globus-M2 spherical tokamak, Nucl. Fusion 62 (10) (2022). ArtNo: № 104002.
[8] G.S. Kurskiev, et al., Energy confinement in the spherical tokamak Globus-M2 with a toroidal magnetic field reaching 0.8 T, Nucl. Fusion 62 (1) (2022) 016011. ArtNo: №.
[9] Yu.V. Petrov, et al., Overview of Globus-M2 spherical tokamak results at the enhanced values of magnetic field and plasm a current, Nucl. Fusion 62 (4) (2022) 042009. ArtNo3.
[10] B.V. Kuteev, E.A. Azizov, P.N. Alexeev, V.V. Ignatiev, S.A. Subbotin, V. F. Tsibulskiy, Development of DEMO-FNS tokamak for fusion and hybrid technologies, Nucl. Fusion 55 (7) (2015) 073035.
[11] P.B. Shchegolev, et al., Neutral beam current drive in Globus-M compact spherical Tokamak, Plasma Phys. Reports 45 (3) (2019) 195–206.
[12] V.K. Gusev, et al., Review of Globus-M spherical tokamak results, Nucl. Fusion 55 (10) (2015). №.
[13] V.V. Dyachenko, et al., The first lower hybrid current drive experiments in the spherical tokamak Globus-M, Nucl. Fusion 55 (2015) 11. №.
[14] Ivanenko S.V., Grinemayera K.A., Puryga E.A., Kvashnin A.N., Bagryansky P.A. Measurement module of dispersion interferometer based on the CO2 laser for plasma density control — Phys. Atomic Nuclei, 2023, Vol. 86, No. 7, pp. 1–10.
[15] T. Akiyama, et al., Recent progress on dispersion interferometers for nuclear fusion and low-temperature plasmas, J. Instrum. 15 (2020) C01004.
[16] A.D. Khil'chenko, A.N. Kvashnin, P.V. Zubarev, D.V. Moiseev, Yu.V. Kovalenko, S. V. Ivanenko, Data Recording System Of A Dispersion Interferometer Based On A CO 2 laser, - Instrum. Experim. Techn 52 (3) (2009) 382–393. №.
[17] J. Tayag Tristan, Watson R. Collins, Digital demodulation of interferometric signals, Modern Metrol. Concerns. — InTech (2012) 317—332.
[18] V. Zaveryaev, et al., Plasma diagnostics. — In: Fusion Physics, International Atomic Energy Agency, Vienna, 2012, p. 360—534.
[19] N.V. Sakharov, A.V. Voronin, V.K. Gusev, A.A. Kavin, S.N. Kamenshchikov, K. M. Lobanov, V.B. Minaev, A.N. Novokhatsky, M.I. Patrov, Yu.V. Petrov, P. B. Shchegolev, Reconstruction of equilibrium magnetic configurations in the Globus-M spherical tokamak, Plasma Phys. Rep. 41 (2015) 997.
[20] M. Greenwald, Density limits in toroidal plasmas, Plasma Phys. Control. Fusion. 44 (8) (2002) R27.
[21] V.V. Bulanin, I.N. Chugunov, M.I. Vildzunas, G.A. Gavrilov, V.K. Gusev, V. B. Minaev, S.V. Krikunov, E.E. Mukhin, Yu.V. Petrov, G.T. Razdobarin, V. V. Rozdestvenskiy, N.V. Sakharov, V.V. Semenov, S.Yu Tolstyakov, A.M. Aronov, Yu.E. Kamach, L.L. Shapiro, A.A. Petrov, V.G. Petrov, S.E. Bender, B.A. Agureev, S. V. Trusillo, The globus-m diagnostics design, Plasma Dev. Oper 9 (1–2) (2001) 129–142, https://doi.org/10.1080/10519990108224492.
[22] G. Kurskiev, et al., Zero-dimensional model to study the effectiveness of plasma heating and thermal energy confinement in globus-M tokamak in ohmic heating modes, Phys. At. Nucl. 80 (7) (2017) 1313–1319.